An XPS and ToF-SIMS study of the passive film formed on a model FeCrNiMo stainless steel surface in aqueous media after thermal pre-oxidation at ultra-low oxygen pressure

Benjamin Lynch, Shova Neupane, Frédéric Wiame, Antoine Seyeux, Vincent Maurice, Philippe Marcus

Benjamin Lynch, Shova Neupane, Frédéric Wiame, Antoine Seyeux, Vincent Maurice, et al.. An XPS and ToF-SIMS study of the passive film formed on a model FeCrNiMo stainless steel surface in aqueous media after thermal pre-oxidation at ultra-low oxygen pressure. Applied Surface Science, 2021, 554, pp.149435. ⟨10.1016/j.apsusc.2021.149435⟩. ⟨hal-03185163⟩

HAL Id: hal-03185163
https://hal.science/hal-03185163v1

Submitted on 30 Mar 2021

An XPS and ToF-SIMS study of the passive film formed on a model FeCrNiMo stainless steel surface in aqueous media after thermal pre-oxidation at ultra-low oxygen pressure

Benjamin Lynch, Shova Neupane, Frédéric Wiame, Antoine Seyeux, Vincent Maurice*, Philippe Marcus**

PSL Research University, CNRS - Chimie ParisTech, Institut de Recherche de Chimie Paris (IRCP), Physical Chemistry of Surfaces Group, 11 rue Pierre et Marie Curie, 75005 Paris, France.

Abstract

A combined X-ray photoelectron spectroscopy, time-of-fight secondary ion mass spectrometry and electrochemical approach was used to investigate the mechanisms of molybdenum and chromium enrichment of a passive film formed on a model austenitic stainless steel single crystal in aqueous acid media and the effect that thermal pre-oxidation at 250 °C plays in the composition, thickness and stratification of the film. A clean FeCrNiMo (100)-oriented surface, prepared under ultra-high vacuum (UHV), was exposed to ultra-low pressures of oxygen at 250 °C, forming a thin oxide film, rich in iron and chromium, as well as containing molybdenum. An argon-filled glovebox, directly attached to the UHV system, allowed for electrochemical alterations to be carried out without exposure to ambient air. After being held at open circuit potential for 30 minutes, hydroxylation of chromium and molybdenum was promoted, with a marked enrichment of both elements in the oxide film. A distinct bilayer film was observed. Anodic polarisation resulted in a significant growth of the inner layer and further enrichment of chromium. Pre-oxidation at 250 °C, using an ultra-low pressure of oxygen, was found to promote protection against transient active dissolution during anodic passivation, and to cause enrichment of molybdenum in the outer layer of the passive film.

Keywords: Stainless steel; corrosion protection; passivation; mechanism; oxide film; XPS; ToF-SIMS

---

1. Introduction

Stainless steels (SS) are widely used in both industry and every day life, from nuclear powerplants to cutlery. They are a versatile and essential material in our society. Our reliance on

---

*Corresponding author email: vincent.maurice@chimieparistech.psl.eu

**Corresponding author email: philippe.marcus@chimieparistech.psl.eu

Preprint accepted for publication: Applied Surface Science – 26/02/2021

stainless steels is due to their remarkable mechanical and corrosion resistance properties. This corrosion resistance is owed to the formation of a protective oxide layer known as the passive film. The film allows the metal alloy to be isolated from its local environment. These thin protective oxide films, of only a few nanometres, are found to be enriched in Cr^{3+} which aids passivity due to its higher stability than Fe^{2+} and Fe^{3+} [1–7]. This effect is further enhanced in acidic media due to iron oxides' higher rate of dissolution [8–11]. Comparatively, in basic media the opposite is observed, where iron oxide is less readily dissolved, causing the enrichment of Cr^{3+} to be less pronounced [8, 12, 13]. In chloride-rich environments the breakdown of the passive film can lead to a phenomenon known as pitting corrosion [14–18], which can cause structural and aesthetic damage, resulting in the potential endangerment of lives and high costs of repair. However, by alloying with small amounts of molybdenum this effect is strongly combated, with molybdenum found in small amounts in the passive film, without increasing the thickness of the film [19–29]. The exact role of molybdenum in fighting against pitting corrosion is a highly debated issue within the community. It is not exactly known whether Mo promotes the repairing of the passive film [22–24] or if Mo prevents the breakdown of the passive film [25–28].

In recent years, it has been found that the distribution of chromium within the passive film is not homogeneous and that these local heterogeneities, which result from the initial growth mechanisms of the oxide film in the pre-passivation stage, may result in the eventual localised breakdown of the passive film [21, 30–35]. It is therefore imperative to better understand the role played by pre-oxidation on the initial stages of passive film formation, as it may improve our knowledge on how we can better combat the localised breakdown and subsequent corrosion.

In the present work, we use surface analysis techniques, combined with electrochemical passivation, to investigate how the controlled pre-oxidation of a model FeCrNiMo austenitic stainless steel single crystal with a (100) orientation, using ultra-low pressure oxygen, affects the stratification, thickness and composition of the passive film. The use of a single crystal model surface allows for a well controlled surface with minimum surface defects, such as grain boundaries and dissimilar crystallographic orientation, meaning that one can more accurately focus on the fundamentals of the mechanisms.

2. Experimental

All experiments were carried out on a (100)-oriented single crystal SS sample (synthesised at École des Mines de Saint-Étienne), which can be considered as a model surface of AISI 316L.

The bulk composition of the alloy was Fe-17Cr-14.5Ni-2.3Mo (at%). Surface preparation and analysis were carried out in an ultra-high vacuum (UHV) platform with an attached glove box. The UHV platform consists of a preparation chamber equipped with a low energy electron diffraction (LEED) system, and separate analysis chambers where X-ray photoelectron spectroscopy (XPS) and scanning tunnelling microscopy (STM) can be performed. As well as housing the LEED system, the preparation chamber is also where the surface can be sputtered by high energy argon ions (up to 5 keV) and annealed to high temperatures (up to 1400 °C) via radiative heating of the backside of the sample. The UHV system operates at a base pressure lower than 1×10^{-10} mbar. The attached glove box, where electrochemistry treatments are carried out, allows for transfer to and from the UHV platform without exposure to ambient air. The glove box is under Ar atmosphere (purity 99.998%, overpressure with respect to atmospheric pressure $\Delta P = 200$ Pa). In the presence of aqueous solutions, necessary for electrochemical treatment, levels of H_2O and O_2 are around 10 and 130 ppm, respectively. An airtight container filled with argon was used to transfer the sample from the glove box to a time-of-flight secondary ion mass spectrometry (ToF-SIMS) system for depth-profiling experiments.

Prior to introduction to the UHV platform, the surface was first mechanically and electrochemically polished, the method for which can be found elsewhere [1, 30]. Once introduced to the UHV system, the sample was subjected to cycles of Ar^+ sputtering ($P_{Ar} = 6.5 \times 10^{-6}$ mbar, 8 μA, 1 keV, 10 minutes) and annealing (700 °C, 10 minutes) in order to create a flat, well ordered surface that is free of contaminants, such as oxygen and carbon. The chemical nature of the surface was verified by XPS, whilst STM and LEED were used to verify the structural state of the surface prior to oxidation. STM imaging shows that the clean surface possesses a $(\sqrt{2} \times \sqrt{2})R45^\circ$ surface structure, similar to that of the one shown by Ma et al. during their investigation of FeCrNi(100) model stainless steel surfaces [36]. Results on the FeCrNiMo(100) surface structure will be reported in detail separately. From here on out this surface will be referred to as the oxide-free surface. The oxide-free surface was initially oxidised at ultra-low pressures (ULP) of oxygen ($P_{O_2} = 7 \times 10^{-8}$ mbar). Gaseous oxygen (99.999% purity) was introduced via a leak valve connected to the analysis chamber in order to oxidise the initial oxide-free surface. The pressure of oxygen in the analysis chamber was continuously recorded and allowed for precise calculation of the total exposure by integrating the pressure as a function of time. The pre-oxidation was carried out once the sample had reached 250 °C, as measured indirectly by a thermocouple. At this temperature it has been found that a crystalline oxide film grows on FeCrNi(100) surfaces [32], with different compositions forming at elevated temperatures [37]. The surface was exposed to O_2 until an oxide layer, containing chromium, iron and molybdenum was formed, as confirmed by XPS. This controlled oxide is defined as the ULP pre-oxidised surface (Stage I). For this set of experiments the ULP pre-oxidised surface was formed after an oxygen exposure of 750 L (1 L = 1.33×10^{-6} mbar $\cdot$ s), ensuring full surface coverage by the oxide. Upon transfer to the Ar-filled glove box, the sample underwent further oxidation due to the presence of residual water vapour and gaseous oxygen (Stage II). The ULP oxide was exposed to this environment for a period of 5 minutes.

The passive oxide films were formed by performing anodic passivation in an electrochemical cell controlled by a Picoscan potentiostat and the corresponding Picoscan software from Agilent Technologies. All treatments were carried out in a home-made Kel-F electrochemical cell [38, 39], capable of holding 350 μL of the 0.05 M H_2SO_4 electrolyte solution, which was prepared using ultra-pure chemicals and Millipore water. Two Pt wires were used as a counter and reference electrode (calibrated as U(SHE) = U(Pt) + 0.75 V). The potential of the Pt reference electrode was stable after thorough cleaning of the cell. The working area was limited by the use of Viton O-ring which provided an area of 0.16 cm^2. For the first electrochemical alteration, the sample was held at open circuit potential (OCP) for 30 minutes (Stage III). The value remained stable at -0.85 V vs Pt for the duration of the 30 minutes. After this alteration and the subsequent analysis by XPS and ToF-SIMS, the sample was anodically passivated for 30 minutes by stepping the potential to -0.1 V vs Pt (Stage IV), a value that is in the mid-range of the passive domain, as shown in the potentiodynamic polarisation curves. A schematic of the procedure to generate the various stages is shown in Figure 1.

Polarisation curves were performed on the as-prepared ULP pre-oxidised surface as well as a surface that had not been pre-treated with ultra-low pressures of oxygen. The latter was sputtered and annealed in the UHV system before being exposed to the glovebox, forming what we define as the native oxide. The polarisation curves were obtained via linear scan voltammetry in the range of -1.1 to $+1.2$ V vs Pt, with a scan rate of 5 $mV{\cdot}s^{-1}$, after resting at OCP for 30 minutes in 0.05 M H_2SO_4. Cathodic pre-treatment was avoided in order to prevent alteration of the previously formed oxide films.

The initial oxide-free surface, oxidised surfaces and subsequent passivation induced alterations were all analysed by XPS. XPS experiments were carried out using an Argus spectrometer and Argus detector, both manufactured by Scienta-Omicron Nanoscience and used a monochromatic Al Kα radiation ($h\nu = 1486.6$ eV) X-ray source. Survey spectra were recorded at a pass energy of

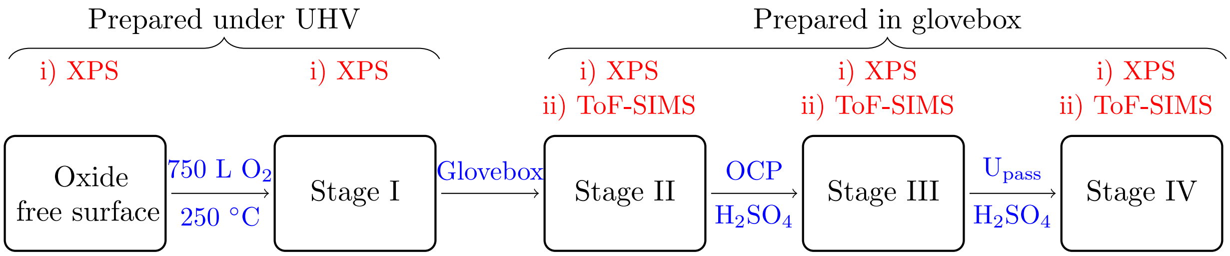

Figure 1: Schematic of experimental procedure.

50 eV and with a step size of 0.5 eV. High resolution spectra of Fe 2p, Cr 2p, Ni 2p, Mo 3d, O 1s, S 2p and C 1s core levels were recorded at a pass energy of 20 eV and with a step size of 0.05 eV. The spectra were recorded at take-off angles of 45° and 90°. Only data for the former are shown. The Fermi level was used as a reference for binding energies. Peak fitting was performed using CasaXPS software [40]. Several constraints, determined using a self-consistent fitting procedure, as well as literature references, were used when fitting the high resolution spectra (full width at half maximum (FWHM), binding energy (BE) and line shape) in order to achieve a more accurate and consistent fit. Relative intensities of the $2p_{3/2}$ and $2p_{1/2}$ spin-orbit doublets of Fe, Cr and S, as well as $3d_{5/2}$ and $3d_{3/2}$ for Mo were fixed according to theoretical ratios; however, only the Ni $2p_{3/2}$ was treated due to no overlap between that and the corresponding Ni $2p_{1/2}$ peak. When there is insufficient gap between spin-orbit peaks, both are fitted in order to fit a more accurate background. Metallic components were fitted with an asymmetric Lorentzian lineshape convoluted by a Gaussian function. For non-metallic peaks, which generally have a less asymmetric shape, a Lorentzian/Gaussian product formula was used in most cases. An adjustable Shirley background was used throughout.

After XPS analysis of each oxidation, or passivation-induced alteration, the sample was transferred to the ToF-SIMS system, before being re-prepared due to the destructive nature of depth-profiling. Depth-profiling elemental analysis was carried out using a ToF-SIMS 5 spectrometer manufactured by Ion ToF. Profiles were recorded with negative secondary ions. The system coupled together the use of static SIMS and sputtering. Static SIMS was carried out using a Bi^+ primary ion source (25 keV, 12 pA, HC-Bunched mode) over an area of 100×100 μm^2. Sputtering was carried out using a Cs^+ sputter beam (0.5 keV, 20 nA) over an area of 300×300 μm^2. Static SIMS was centred in the sputtered crater in order to avoid edge effects.

3. Results and Discussion

3.1. Electrochemical passivation.

Figure 2 compares two polarisation curves obtained on the FeCrNiMo(100) surface, one after pre-oxidation using ULP conditions at 250 °C and the second after being directly transferred to the Ar-filled glovebox at room temperature. The two oxidised surfaces show the same corrosion potential, where $U_{corr}=-0.8 \pm 0.01$ V/Pt. This is expected for the same sample that is fully covered by surface oxide. The cathodic branches of the polarisation curves show a similar shapes; however, the ULP pre-oxidised sample has a lower current density, indicating a slightly decreased proton reduction activity in the electrolyte. Similar behaviour in the cathodic branches has been previously reported [35].

The anodic branch shows that the current density of the ULP prepared surface is comparatively lower at the active-passive transition than that of the native oxide covered surface prior to passivation and with clear suppression of the active peak. Similar observations have previously been made when comparing native oxide covered and room temperature pre-oxidised ULP surfaces on polycrystalline 316L samples [38]. We can therefore deduce that the ULP pre-oxidised sample, prepared at 250 °C and exposed to an acidic electrolyte, is fully protected against active dissolution, much like the ULP pre-oxidised samples prepared at room temperature, whilst the native oxide covered samples, formed in air or an Ar-filled glovebox, remain only partially protected.

If one compares the densities of anodic charge transferred in the potential range of the active-passive transition, defined as U_{corr} to $U_{corr}+0.2$ V, we obtain values of 0.265 and 0.458 $\mathrm{mC{\cdot}cm^{-2}}$ for the ULP pre-oxidised and native oxide covered samples, respectively. From the charge transfer difference (0.193 $\mathrm{mC{\cdot}cm^{-2}}$), if one then assumes that the charge is completely associated with metal dissolution and that all elements dissolve as $\mathrm{M \rightarrow M^{2+} + 2\,e^{-}}$, then we can estimate the amount of metal that was additionally lost by transient active dissolution in the case of the native oxide. By taking into account that the thickness of the (100) plane for the *fcc* structure of the alloy is 0.18 nm, and that the atomic density is 1.55×10^{15} $\mathrm{at{\cdot}cm^{-2}}$, we arrive at a value of 0.07 nm, not taking account the stoichiometry of dissolution, which corresponds to less than one monolayer (0.38 ML) of additionally consumed metal. In the case of the polycrystalline sample [38], the charge transfer difference at the active-passive transition was reported as 0.38 $\mathrm{mC{\cdot}cm^{-2}}$, twice the amount of the present case, which yields a value of 0.76 ML of additionally consumed metal for the native oxide-covered sample, assuming a (100) orientation for the calculation. Therefore, we can say that

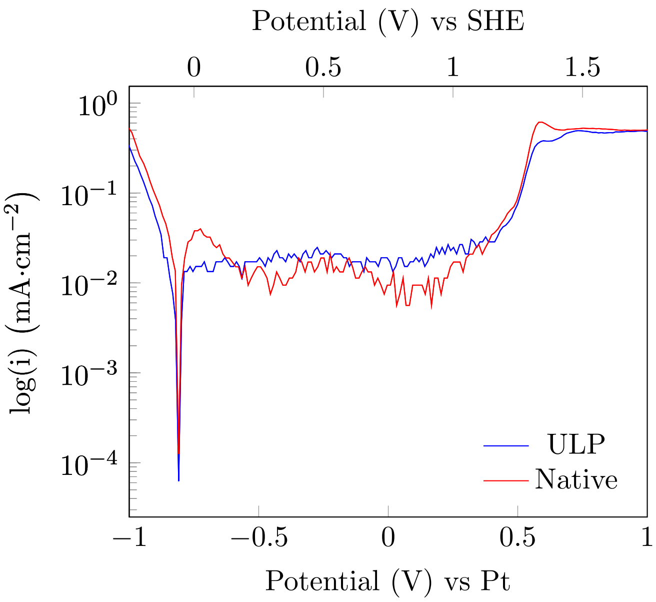

Figure 2: Polarisation curves of a Fe-17Cr-14.5Ni-2.3Mo (100)-oriented model stainless steel surface prepared oxide-free in UHV and subsequently pre-oxidised by exposure to ultra-low pressures of oxygen (ULP, blue) or via exposure to the glovebox environment (Native, red).

the presence of ULP and native oxide films provides protection and pre-passivation at OCP on both FeCrNiMo single and 316L poly crystalline samples. However, it is evident that ULP pre-oxidation treatment, whether performed at moderate (250 °C) or room temperature, promotes an enhanced protectiveness against active dissolution owed to more efficient blocking of the residual transient active dissolution upon anodic passivation.

In the passive domain we observe a slightly higher current density for the ULP pre-oxidised surface although the difference between it and that of the native oxide is within the range of reproducibility. It should be noted that entrance into the transpassive region is met with an activation peak in the case of the native oxide, which is not the case for the ULP oxide. Other than that behaviour in this region is similar.

In the following, we will focus the discussion on the surface composition and stratification of the ULP sample, thermally pre-oxidized at 250 °C, and the effects of electrochemical passivation.

3.2. XPS fitting parameters

XPS fitting parameters, in line with those used in previous work [38], for the Mo 3 $d_{5/2}$, Cr 2 $p_{3/2}$, Fe 2 $p_{3/2}$, Ni 2 $p_{3/2}$, O 1 s, S 2 $p_{3/2}$ and S 2 s peaks are found in Table 1. Parameters were obtained by applying a self-consistent fitting approach as well as with reference to the literature [29, 35, 37].

Core level	State	Assignment	BE (± 0.1 eV)	FWHM (± 0.1 eV)	Asymmetry Index
Mo 3 $d_{5/2}$	Mo^0	Metal	227.6	0.6	0.37
	Mo^{4+}	Oxide	229.1	1.3	0.25
	Mo^{4+}	Hydroxide	231	1.5	0.25
	Mo^{6+}	Oxide	232.3	1.6	0.00
Cr 2 $p_{3/2}$	Cr^0	Metal	573.8	1.1	0.57
	Cr^{3+}	Oxide	576.6	2.4	0.28
	Cr^{3+}	Hydroxide	577.4	2.0	0.34
	Cr^{3+}	Oxide satellite	588.5	5.4	0.00
	Cr^{3+}	Hydroxide satellite	589.6	5.4	0.00
Fe 2 $p_{3/2}$	Fe^0	Metal	706.9	0.8	0.60
	Fe^{2+}	Oxide	708.3	1.6	0.31
	Fe^{3+}	Oxide	710.3	3.1	0.42
	Fe^{3+}	Hydroxide	711.8	3.7	0.00
	Fe^{2+}	Satellite	712.8	3.8	0.13
	Fe^{3+}	Satellite	716.3	4.2	0.21
Ni 2 $p_{3/2}$	Ni^0	Metal	852.8	0.9	0.36
	Ni^0	Satellite	859.0	4.0	0.00
O 1 s	O^{2-}	Lattice oxide	530.2	1.2	0.00
	OH^-	Hydroxide	531.4	1.6	0.00
	${SO_4}^{2-}$	Sulphate	532.1	1.4	0.00
	H_2O	Water	533.0	2.3	0.00
S 2 $p_{3/2}$	${SO_4}^{2-}$	Sulphate	169.1	1.3	0.00
S 2 s	${SO_4}^{2-}$	Sulphate	233.1	1.5	0.00

Table 1: XPS peak fitting parameters obtained for reconstruction of spectra.

Spin orbit splitting between Mo 3 $d_{5/2}$ and Mo 3 $d_{3/2}$ was found to be 3.2 eV for all peaks except for Mo^{4+} ((oxy)hydroxide), which was 3.3 eV. These values are in line with those reported in the literature [33, 41, 42]. Values for spin orbit splitting between Cr 2 $p_{3/2}$ and Cr 2 $p_{1/2}$ were 9.4 eV, 9.8 eV, 9.7 eV, 9.0 eV, 9.3 eV for Cr^0, Cr^{3+} (oxide), Cr^{3+} (hydroxide), Cr^{3+} (oxide satellite) and Cr^{3+} (hydroxide satellite), respectively. Similar splitting energies for these species have been reported in the literature [37, 43, 44]. For the spin orbit splitting between Fe 2 $p_{3/2}$ and Fe 2 $p_{1/2}$ differences of 13.0 eV, 13.5 eV, 13.3 eV, 12.9 eV, 13.4 eV and 13.5 eV were found for Fe^0, Fe^{2+} (oxide), Fe^{3+} (oxide), Fe^{3+} (hydroxide), Fe^{2+} (satellite) and Fe^{3+} (oxide satellite), respectively. Similar values are reported within the literature [37, 44]. Spin orbit splitting between S 2 $p_{3/2}$ and S 2 $p_{1/2}$ was 1.2 eV, as widely reported in the literature [45–47].

3.3. XPS analysis

The fitted XPS spectra for each stage are shown in Figure 3, with the corresponding relative intensities shown in Table 2. Firstly, looking at the changes in the chromium during the alterations, the ULP pre-oxidised (Stage I) surface shows only Cr^0 and Cr^{3+} in its oxide form, which is almost certainly Cr_2O_3, as widely reported in the literature [35, 36, 39]. The ratio of Cr^0/Cr^{3+} is 0.85. For the sake of clarity, satellite peaks corresponding to a given oxidation state are included in the quantification results. After exposure to the GB environment (Stage II), which as previously stated contains residual water vapour and oxygen, we observe further oxidation of the chromium metal to Cr^{3+}, with the ratio of Cr^0/Cr^{3+} now being 0.35. After undergoing the first electrochemical treatment where the sample was held at OCP (−0.85 V vs Pt) for 30 minutes (Stage III), we observe a hydroxide species become the dominant chromium state. Literature reports suggest that this hydroxide is most likely $Cr(OH)_3$ [1, 30, 33–35]. Once again, we observe the decrease in the amount of metal measured at the surface. The ratio of Cr^0/Cr^{3+} is now 0.25. This is not a significant decrease relative to the amount of hydroxide now present, indicating that the oxide is hydroxylated rather than the metal. The ratio of oxide/hydroxide is calculated as 0.40. Upon anodically passivating the sample (−0.1 V vs Pt) for 30 minutes (Stage IV), the trend of a decreasing metal concentration is continued, with the of Cr^0/Cr^{3+} now 0.09. However, the ratio of oxide/hydroxide is increased to 1.40, confirming the promoting effect of anodic polarization on dehydroxylation [1, 30, 33–35, 48].

Moving on to the analysis of the iron XPS spectra (Figure 3b), and with reference to Table 2, we once again start by looking at the ULP pre-oxidised surface. The calculated ratio of metal to total

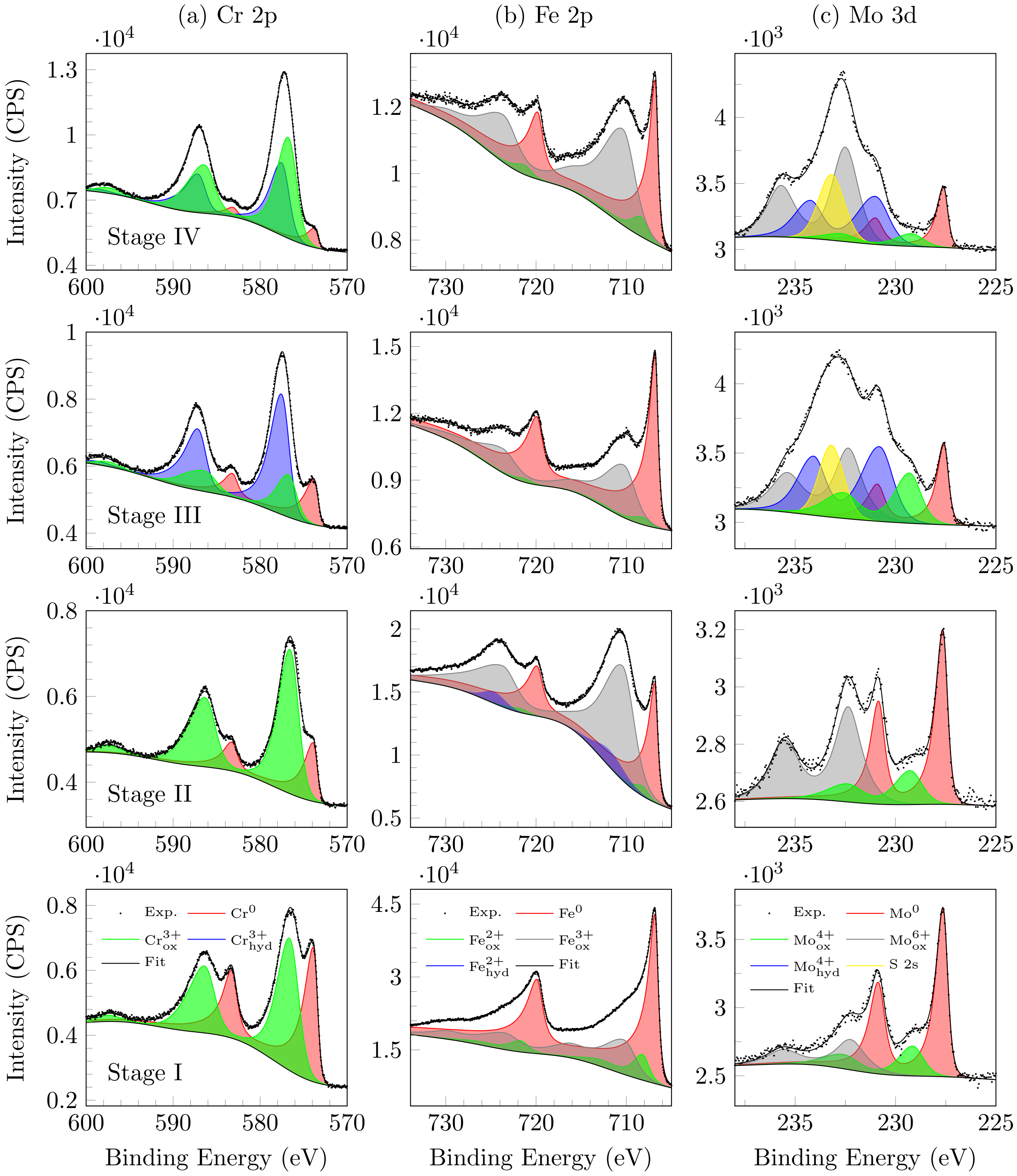

Figure 3: (a) Cr 2p, (b) Fe 2p and (c) Mo 3d XPS spectra and peak fitting of a Fe-17Cr-14.5Ni-2.3Mo (100)-oriented model stainless steel after forming a surface oxide using ultra-low pressures of pure oxygen (750 L, 250 °C) (I), after exposure of the ULP oxide to the Ar-filled glovebox (II), and then after the previous stage undergoes treatment in 0.05 M H_2SO_4 at OCP (III), and finally after the previous stage has been passivated via anodic polarisation at −0.1 V in the passive domain (IV).

Stage	Relative Intensity (±2%)													
	Fe				Cr			Mo				Ni*		
	Fe^0	Fe^{2+}_{ox}	Fe^{3+}_{ox}	Fe^{3+}_{hyd}	Cr^0	Cr^{3+}_{ox}	Cr^{3+}_{hyd}	Mo^0	Mo^{4+}_{ox}	Mo^{6+}_{ox}	Mo^{4+}_{hyd}	Ni^0	Ni^{2+}_{ox}	Ni^{2+}_{hyd}
I	65	9	26	0	46	54	0	64	15	21	0	100	0	0
II	33	3	55	9	26	74	0	43	15	42	0	93	7	0
III	65	3	32	0	20	23	57	17	19	28	36	100	0	0
IV	43	5	52	0	8	54	38	17	7	46	30	100	0	0

Table 2: Relative intensity of Fe, Cr, Mo and Ni in metallic, oxide and hydroxide states after different surface preparations. *Uncertainty associated with quantification of nickel is ±5% so small amounts of nickel (hydr)oxide cannot be excluded.

oxide is 1.9, which is much higher than the corresponding Cr^0/Cr^{3+} at the same stage, indicating that iron is less readily oxidised than metallic chromium during the early stages of oxidation. There are two oxides of iron present, Fe^{2+} and Fe^{3+}, alongside the metal. It is not possible to define an exact composition of these iron oxides using XPS; however, the main oxides are often cited as Fe_3O_4, Fe_2O_3 and FeO. Work by Grosvenor et al. [49] suggests that FeO does not form at exposures lower than 10^4 L, which is contrary to other reports suggesting that FeO exists as a nucleating oxide at low exposures [37, 50–52]. After exposure to the glove box, more of the metal at the surface is oxidised and Fe^{3+} becomes the dominant species. The spectrum suggests that Fe^{2+} oxide is still present, albeit in a reduced amount. It should be noted that we also observe the presence of a new peak corresponding to that of an iron hydroxide species at 711.8 eV. The metal/(hydr)oxide ratio is 0.49, indicating the large decrease in the amount of metal at the surface after exposure to the glove box environment for 5 minutes. After the first electrochemical alteration where the sample was held at OCP for 30 minutes, we no longer observe a hydroxide peak. It is also interesting to note that we see a resurgence in the amount of iron metal at the surface relative to the amount of oxide, with a metal/oxide ratio of 1.9, which is the same ratio as previously seen after forming the ULP pre-oxidised surface. This is due to the dissolution of iron oxides in acidic media, which is in agreement with previous studies after OCP exposure where a closed system for transfer to surface analysis was used [34, 35, 38, 48]. The main difference between these two oxide layers is that after the electrochemical treatment, we observe a much larger proportion of Fe^{3+} to Fe^{2+} than after the ULP pre-oxidation treatment. For the ULP pre-oxide we have a ratio of 2.9 for

Fe^{3+}/Fe^{2+}, whereas after the first electrochemical alteration it is increased to ≈ 10. After the final electrochemical treatment, where the sample was anodically passivated, there is a reduced amount of metal, which was also observed in the chromium, now with almost equal amounts of metal and oxide (metal/oxide = 0.76). Once again no more iron hydroxide is observed. The change in the ratio between Fe^{3+} and Fe^{2+} is found to be insignificant.

Much like that of iron, the analysis of molybdenum is complex, owed to a variety of molybdenum species present as well as the sulphur 2s peak overlapping with this region of the spectrum after treatment involving H_2SO_4 as an electrolyte. The relative intensities of molybdenum are shown in Table 2. Unlike iron, it is not subject to complicated satellite peaks. The ULP pre-oxide spectrum shows a mixture of molybdenum metal and two oxides with different oxidation states, Mo^{4+} and Mo^{6+} [29, 34, 53, 54]. Mo^{6+} exists as two different oxides which cannot be differentiated by XPS, although $[MoO_4]^{2-}$ is found to be more stable than MoO_3 in acidic electrolytes [55]. The ratio of metal to total oxide is 1.8. The amounts of Mo^{4+} and Mo^{6+} are almost 3:4. After exposure to the glove box, we observe a large increase in the amount of Mo^{6+}. It is now the dominant oxide with there now more than double the amount present compared to Mo^{4+}. The ratio of metal/oxide has also fallen more than 2 fold, to 0.75. It is after the electrochemical treatments that things become more complex when treating the data due to the introduction of the sulphur 2s peak and Mo^{4+} (oxy)hydroxide. The introduction of the hydroxide comes at the same stage as that of $Cr(OH)_3$. The area, A, of the sulphur 2s peak was fixed according to the corresponding area of the sulphur 2p region, as

$$A_{2s} = A_{2p} \frac{\sigma_{2s} \cdot T_{2s} \cdot \lambda_{2s} \cdot \left(1 - e^{-\frac{d}{\lambda_{2s} \sin\theta}}\right)}{\sigma_{2p} \cdot T_{2p} \cdot \lambda_{2p} \cdot \left(1 - e^{-\frac{d}{\lambda_{2p} \sin\theta}}\right)},$$

where the values for the photoionisation cross section, σ, the transmission of the analyser, T, the inelastic mean free path, λ, and the angle of photoemission, θ, are known, and the thickness of the layer, d, is calculated. The ratio of metal/(hydr)oxide continues its downward trajectory at a value of 0.19, a similar behaviour to that of chromium and contrary to that of iron. The hydroxide peak is significant and, as a percentage of the molybdenum concentration, it is the most common species. After passivation, we observe a reduction in the amount of hydroxide present, again showing similar behaviour to chromium. Similar behaviour has been witnessed on a polycrystalline 316L sample after room temperature pre-oxidation [38]. Mo^{4+} is at its lowest concentration of the process whilst Mo^{6+} has increased its share of the concentration, indicating that it is enriched in the passive film.

It is worth noting that whilst nickel is a significant element in the alloy (14.5 at%), at no point in the procedure is its oxidised form detected as a significant amount by XPS. After being introduced to the glove box environment it is only present in small amounts at the surface.

3.4. ToF-SIMS analysis

The negative ion depth profiles for the sample through stages II to IV are shown in Figure 4, with the secondary ions of $^{18}O^-$, $^{18}OH^-$, $CrO_2{}^-$, $FeO_2{}^-$, $NiO_2{}^-$ and $MoO_3{}^-$ attributed to the oxide film, and $Cr_2{}^-$, $Fe_2{}^-$ and $Ni_2{}^-$ assigned to the metallic substrate. The very weak signal from $Mo_2{}^-$ is ignored. When selecting negative ions for analysis of the metallic substrate, masses corresponding to those of metallic clusters, $M_2{}^-$, were preferred over single metal anions, M^-, as it reduces the possibility of a contribution to the signal from a metal ion that originated as an oxide species. Similar reasoning can be used to explain the decision to select $MO_2{}^-$ over MO^- – there is a lower probability of 2 oxygen atoms recombining with a metal atom originating from the metallic substrate than 1 oxygen atom and one metal atom. $MoO_3{}^-$ is selected over $MoO_2{}^-$ simply due to a higher intensity. This process allows for more certainty in assigning the ion to the corresponding species. Depth profile analysis of Stage I, the ULP oxide, is not possible as in order to transport the sample to the ToF-SIMS platform it is necessary to go via the glovebox, which further oxidises the sample before analysis is possible. Along with the oxide film itself, we can also define a region corresponding to the modified alloy; it is widely reported that we observe an enrichment of metallic nickel in austenitic and duplex stainless steels in the region between the metallic substrate and the oxide film [24, 30, 34, 56]. The position of the modified alloy-oxide interface will be defined by the maximum intensity of $Ni_2{}^-$ ions and is indicated by a dashed line. Estimations made using ToF-SIMS suggest that the thickness of this modified alloy region is of the same magnitude as that of the oxide film.

Looking at the ToF-SIMS depth profile for Stage II, after exposure to the glovebox, the maximum intensity attributed to $CrO_2{}^-$ ions is at 34 s, whilst the maximum of the $FeO_2{}^-$ and $MoO_3{}^-$ ions is at 14 s and 8 s, respectively. It should be noted that, due to the noise associated with the spectra, these times are taken using the median value from a small range, typically no greater than ± 3 s (depending on the shape of the curve), in which the intensity is at its highest point. This result indicates an inhomogeneous distribution of chromium oxide in the film, with an enrichment close to the metal substrate-oxide interface, as previously reported for native oxides formed on 316L SS in air [33, 34, 57]. Whilst we observe maxima for the Fe and Mo oxide ions at 8–14 s, the shape of the curves suggest a more homogeneous distribution within the layer with a more

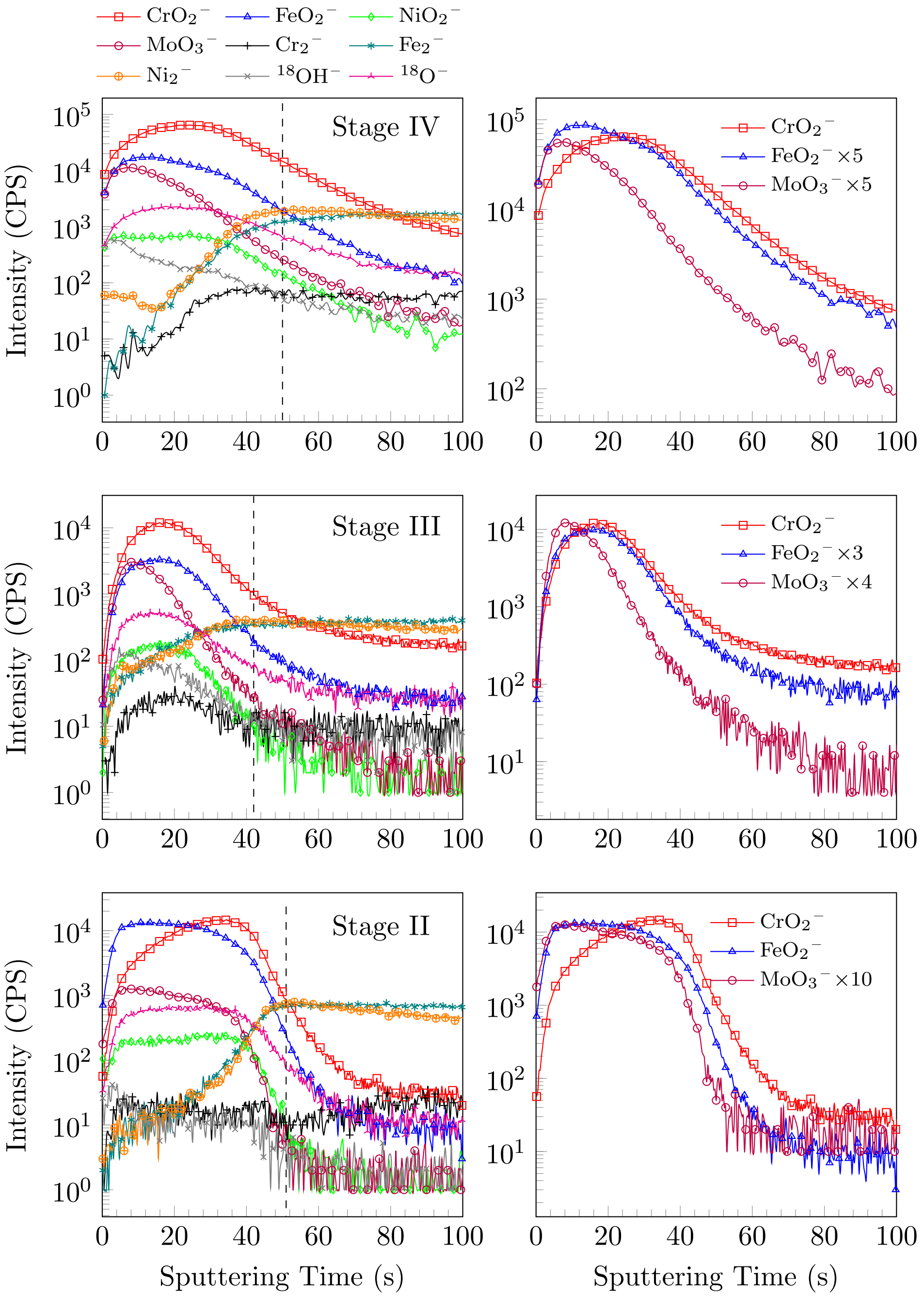

Figure 4: ToF-SIMS negative ion depth profiles for stages II–IV of the treatment of a Fe-17Cr-14.5Ni-2.3 (100)-oriented model stainless steel: (left) CrO_2^-, FeO_2^-, NiO_2^-, MoO_2^-, Cr_2^-, Fe_2^-, Ni_2^-, $^{18}OH^-$ and $^{18}O^-$ secondary ions, (right) Only CrO_2^-, FeO_2^- and MoO_3^- secondary ions. The dashed line indicates the position of the oxide-modified alloy interface, determined by the maximum of the Ni_2^- profile.

pronounced presence of molybdenum oxides in the outer part of the film, which has also been the case for other films formed on 316L stainless steels in air [33, 34, 57]. The depth profile shows the presence of NiO_2^- ions throughout the oxide layer, suggesting that there is in fact a nickel oxide distributed in the film, however, it will only be present in a very small quantity as indicated by the XPS data. This can be explained by acknowledging that ToF-SIMS is highly sensitive to trace amounts which can be below the detection limit of XPS. Comparing the distribution of $^{18}OH^-$ and $^{18}O^-$, we can see that the former peaks very early at 4 s and then rapidly declines, whilst the latter is more homogeneously distributed, with its maximum at 26 s. At this stage XPS suggests that the only hydroxide present is that of iron, which is evidence of the early formation of the well-reported bilayer structure of the passive films formed on stainless steel, with an inner oxide barrier layer and an outer exchange layer [30, 33, 34, 58, 59]. Using the previously mentioned definition for the modified alloy, where the metallic nickel intensity is at its maximum, we can state that it begins at the 51 s mark. The curve then slowly decreases, suggesting an enrichment of nickel underneath the oxide film, which is confirmed by surface composition analysis presented below.

Moving on to the depth profile for Stage III, the first thing to note is the clear shift to a lower sputtering time (relative to the other ions) of the maximum intensity of CrO_2^-, now at 17 s, whilst the maxima for FeO_2^- and MoO_3^- are at 14 s and 9 s, respectively. As already evidenced by XPS, at this stage there is a large amount of chromium hydroxide present, which has previously been shown to be in the outer layer of the oxide film [33–35]. The result is a broader curve for the CrO_2^- ions, indicating a more homogeneous distribution of oxidised chromium within the now thinner film. MoO_3^- ions also exhibit a shift to a lower sputtering time relative to that of the iron ions, partly due to the formation of molybdenum hydroxide near the outermost surface, and partly due to the loss of iron oxide via dissolution in the acidic medium. At this stage, according to the XPS data, we witness the presence of a molybdenum based hydroxide, which will be present in the extreme outer portion of the film. Once more we see the same behaviour when comparing $^{18}OH^-$ and $^{18}O^-$, with an early peak and subsequent decline for the hydroxide, whilst oxide ions peak slightly later but with a shallower decline, confirming the bilayer structure of the passive film. In this case, the modified alloy region is shown to begin after 42 s, which is a reduction in time compared to Stage II, indicating a likely reduction in the thickness of the oxide, providing that we assume a close to constant sputtering yield. This is not surprising as XPS data showed that there is a significant loss of iron oxide caused by its preferential dissolution in acidic media. This effect has been noted on an array of stainless steel surfaces whether oxidised in air or using a controlled

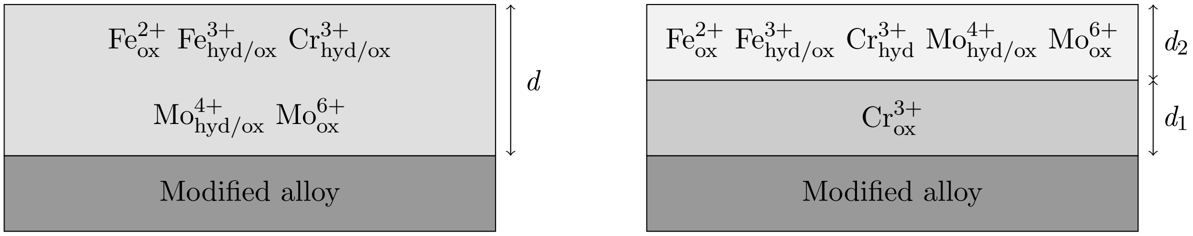

Figure 5: Single-layer (left) and bilayer (right) models of the surface oxide film formed on FeCrNiMo stainless steel.

pre-oxidation [33–35, 38].

Moving on to Stage IV, after the sample had been stepped to the anodic passivation potential for 30 minutes, we note a shift to an increased sputtering time for the maximum of the curve (26 s) corresponding to that of CrO_2^- ions. This is due to the dehydroxylation of the chromium into Cr_2O_3, which is present in the inner part of the oxide film. The maximum intensity of both the FeO_2^- and MoO_3^- ions remains similar to as seen in stage III, with maxima of 13 s and 8 s, respectively. The position of the modified alloy is shifted to a higher sputtering time, now beginning after 50 s, indicating a possible significant growth in the oxide film when compared to Stages II and III, which can be investigated using XPS thickness estimations. Similar observations have previously been made when investigating room temperature oxidation in air and ultra-low pressures of oxygen [33–35, 38].

3.5. Film thickness and composition

XPS intensities can be used to calculate the thickness of oxide films and the distribution of elements within them [1, 21, 30, 33, 35, 57, 60–63]. To do this we must select a model that makes the assumptions that the oxide film has homogeneous, continuous and flat layers. For this work, two different systems have been modelled – firstly, a single layer model which assumes a homogeneous distribution of all the oxides and hydroxides, and secondly, a bilayer model which assumes a hydroxide rich outer exchange layer with the electrolyte and an inner barrier chromium oxide layer. From the ToF-SIMS data, as well as XPS angular measurements, we feel that the assignment of Cr^{3+} to the inner layer and the remaining species to the outer, is closer to reality than the single layer model. The presence of iron and molybdenum in their low oxidation state cannot be excluded from the inner barrier layer. The two systems are shown in Figure 5.

Results from the calculations for the thickness and composition of the oxide layer utilising the single-layer model are shown in Table 3. The oxide layers range from 0.9–2.1 nm in height, with the passive film being at mid-range for typical estimates for passive films formed on stainless steel, which are typically 1–3 nm in thickness [1, 19, 22, 25, 30, 33–35, 38, 64, 65]. The ULP formed oxide is very thin and found to be slightly enriched in iron and chromium relative to the modified alloy of the oxide free surface, whilst molybdenum has the same concentration as its bulk amount. Upon introduction to the glovebox we observe the growth of the film, with it almost doubling in thickness. The composition of the oxide film remains very similar. We also confirm a slight enrichment of nickel in the modified alloy, which had already been indicated by ToF-SIMS results and is in agreement with many previous studies [1, 30, 33–35, 38, 57, 65]. Post-oxidation one observes a significant decrease in the relative concentration of metallic chromium in the modified alloy, which remains lower than that of the clean surface throughout the duration of the experimental set. Ma et al. have reported similar decreases in the amount of chromium in the modified alloy after room temperature ULP oxidation of FeCrNi alloys [35]. Conversely, when investigating passive films formed from native oxides on freshly polished polycrystalline 316L surfaces, Wang et al. showed no significant change in the amount of chromium present in the modified alloy [33]. This suggests that ULP pre-oxidation of clean and well-ordered surfaces may affect the transportation of metallic chromium under the oxide layer when compared with oxides formed after exposure to ambient air and may be investigated further. After the first electrochemical treatment we observe a reduction in the thickness of the film and a marked decrease in the amount of iron, which confirms the dissolution of iron oxide in acidic media. Molybdenum and chromium are found to be markedly enriched in the film, at approximately four and six times the amount of the initial oxide-free surface, respectively. Upon passivating the surface, we observe an increase in the thickness of the film, with chromium enriched even further. This growth is owed to the applied anodic polarization which forces a faster formation of oxide species, counteracting the oxide dissolution. A reduction in the molybdenum enrichment is observed, however, it remains at three times the amount of the initial oxide free surface. There is a notable increase in the amount of nickel present in the modified alloy. The amount of metallic molybdenum is the same as that of the oxide-free surface, indicating that there is no depletion of the modified alloy region.

Results from the calculations for the thickness and composition of the oxide layers for the bilayer model are shown in Table 4. It should be noted that the results for the modified alloy are identical using both layer models, so it is therefore not repeated in Table 4. After the ULP oxide has been transferred to the glovebox both layers grow, doubling in thickness, with no apparent change in the concentration of iron and molybdenum in the outer layer. XPS results indicated that iron hydroxide would also be present in the outer layer after stage II. It is after stage III that we observe

Stage	Thickness d (nm)	Relative concentration (± 2%)						
		Oxide layer			Modified alloy			
		Fe	Cr	Mo	Fe	Cr	Ni	Mo
Oxide free	–	–	–	–	76	14	7	2
I	0.9 (±0.1)	79	19	2	80	7	12	1
II	1.7 (±0.2)	82	16	2	74	9	16	1
III	1.4 (±0.2)	37	51	12	71	11	16	2
IV	2.1 (±0.2)	37	57	6	67	9	22	2

Table 3: Thickness and composition of oxide layer and modified alloy using the single-layer model as calculated from XPS data.

an overall decrease in the thickness of the oxide and a significant enrichment of chromium and molybdenum in the outer layer, caused by the dissolution of iron in the acidic electrolyte leading to a decrease in the thickness of the outer layer. Molybdenum makes up approximately 14% of the outer layer, a 7 fold increase relative to the amount present on oxide free surface. This large enrichment of molybdenum is likely to have a beneficial effect on the transient anodic dissolution at the active/passive transition, as shown by the electrochemical data discussed above, which is of importance when it comes to self-repair of the film after passivity breakdown [22, 30, 34, 38]. The inner layer is also found to decrease slightly, suggesting that the chromium oxide previously present is in fact hydroxylated. After stage IV, where the sample is anodically passivated in H_2SO_4, the outer layer is not found to grow; however, a remarkable increase in the thickness of the inner layer is observed, with it found to treble in height. This significant increase in thickness of the inner barrier layer has not previously been observed on other passive films that have been pre-oxidised at room temperature prior to passive film formation in an acidic electrolyte [34, 38]. The XPS analysis above showed that, in the case of chromium, the oxide:hydroxide ratio increased significantly, from 0.40 to 1.40 after passivation. The loss of thickness caused by the dehydroxylation of chromium in the outer layer is counter acted by the further oxidation of iron metal, which may explain the decrease in the relative concentration of iron in the modified alloy. The relative concentration of molybdenum in the outer layer is found to decrease, although it remains significantly enriched relative to that of the oxide-free modified alloy. In our previous study that investigated how a room temperature pre-oxidation of a polycrystalline 316L stainless steel further enriched the amount of

Stage	Thickness d (nm)			Relative concentration of outer layer (± 2%)		
	Total (±0.1)	Outer layer	Inner layer	Fe	Cr	Mo
I	0.9	0.7	0.2	98	0	2
II	1.8	1.4	0.4	98	0	2
III	1.5	1.2	0.3	44	42	14
IV	2.1	1.2	0.9	55	35	10

Table 4: Thickness and composition of oxide layers using the bilayer model as calculated from XPS data. The composition of the inner layer is always 100% chromium.

molybdenum [38], we found a 19% relative concentration of the outer layer of the film after anodic passivation, versus 10% in the present study, the same value as for the native oxide pre-covered polycrystal 316L after it had been submitted to anodic passivation. Molybdenum plays a significant role in the stability of the oxide in the passive range, so we can suggest that larger amounts in the outer layer would enhance the resistance to breakdown of the passive film. So by comparing with work done on the room temperature ULP pre-oxidation of a polycrystalline 316L surface, where the enrichment of molybdenum is found to increase after being anodically passivated, it would suggest that high temperature pre-oxidation results in a lower stability in the passive range than when the pre-oxidation is carried out at room temperature. Evidently there are several other factors that will play a role and this requires further investigation. Overall, this work confirms that controlled pre-oxidation under ultra-low oxygen pressure is instrumental to promote the Mo enrichment in the passive film. It also suggests that the temperature of pre-oxidation may play an important role in the subsequent performance of the passive film formed in aqueous acid electrolytes.

4. Conclusion

High resolution XPS and ToF-SIMS depth profiling analysis were used to investigate the effect of thermal ULP pre-oxidation at 250 °C on the composition and structure of the passive film formed in a 0.05 M H_2SO_4 electrolyte, on a (100)-oriented FeCrNiMo model stainless steel surface.

ULP pre-oxidation was found to improve the protectiveness of the surface oxide film at the active-passive transition when compared with the native oxide formed on the same surface. The ULP and glovebox formed oxides were found to be enriched in iron which later dissolved into the acidic electrolyte after being held at OCP, resulting in the enrichment of chromium and molybdenum in the film. Anodically passivating the surface caused growth of the film and favoured dehydroxylation of both chromium and molybdenum. It was found that thermal ULP pre-oxidation promoted the enrichment of molybdenum in the passive film, albeit not as significantly when compared with previous experiments that investigated the effect of a room temperature ULP pre-oxidation on 316L polycrystalline stainless steel [38]. This would suggest that thermal ULP pre-oxidation is likely to improve the self-repairing properties of the passive film, and its resistance to breakdown, although not more than a ULP pre-oxidation carried out at room temperature. However, it was found that relative to these previous studies, ULP pre-oxidation 250 °C caused an enhancement in the growth of the chromium inner oxide layer after anodic passivation, which will influence the transport of ions through the passive film.

Acknowledgements

This project has received funding from the European Research Council (ERC) under the European Union's Horizon 2020 research and innovation program (ERC Advanced Grant No. 741123, Corrosion Initiation Mechanisms at the Nanometric and Atomic Scales : CIMNAS). Région Île-de-France is acknowledged for partial funding of the UHV equipment.

References

[1] V. Maurice, W. Yang, P. Marcus, X-Ray photoelectron spectroscopy and scanning tunneling microscopy study of passive films formed on (100) Fe-18Cr-13Ni single-crystal surfaces, Journal of the Electrochemical Society 145 (3) (1998) 909–920.

[2] D. D. Macdonald, Passivity–the key to our metals-based civilization, Pure and Applied Chemistry 71 (6) (1999) 951–978.

[3] I. Olefjord, B.-O. Elfström, The composition of the surface during passivation of stainless steels, Corrosion 38 (1) (1982) 46–52.

[4] P. Marcus, Corrosion mechanisms in theory and practice, CRC press, 2011.

[5] P. Schmuki, From bacon to barriers: a review on the passivity of metals and alloys, Journal of Solid State Electrochemistry 6 (3) (2002) 145–164.

[6] J. W. Schultze, M. Lohrengel, Stability, reactivity and breakdown of passive films. Problems of recent and future research, Electrochimica Acta 45 (15-16) (2000) 2499–2513.

[7] M. Liu, X. Cheng, X. Li, Y. Pan, J. Li, Effect of Cr on the passive film formation mechanism of steel rebar in saturated calcium hydroxide solution, Applied Surface Science 389 (2016) 1182–1191.

[8] N. Sato, T. Noda, K. Kudo, Thickness and structure of passive films on iron in acidic and basic solution, Electrochimica Acta 19 (8) (1974) 471–475.

[9] G. Burstein, P. Marshall, The coupled kinetics of film growth and dissolution of stainless steel repassivating in acid solutions, Corrosion Science 24 (5) (1984) 449–462.

[10] K. Asami, K. Hashimoto, S. Shimodaira, An XPS study of the passivity of a series of iron—chromium alloys in sulphuric acid, Corrosion Science 18 (2) (1978) 151–160.

[11] M. Bojinov, I. Betova, G. Fabricius, T. Laitinen, T. Saario, et al., The stability of the passive state of iron–chromium alloys in sulphuric acid solution, Corrosion Science 41 (8) (1999) 1557–1584.

[12] G. Burstein, P. Marshall, Growth of passivating films on scratched 304L stainless steel in alkaline solution, Corrosion Science 23 (2) (1983) 125–137.

[13] S. El-Egamy, W. Badaway, Passivity and passivity breakdown of 304 stainless steel in alkaline sodium sulphate solutions, Journal of Applied Electrochemistry 34 (11) (2004) 1153–1158.

[14] P. Marcus, V. Maurice, H.-H. Strehblow, Localized corrosion (pitting): A model of passivity breakdown including the role of the oxide layer nanostructure, Corrosion Science 50 (9) (2008) 2698–2704.

[15] G. Frankel, Pitting corrosion of metals: a review of the critical factors, Journal of the Electrochemical Society 145 (6) (1998) 2186.

[16] M. Streicher, Pitting corrosion of 18Cr-8Ni stainless steel, Journal of the Electrochemical Society 103 (7) (1956) 375.

[17] S. Refaey, F. Taha, A. Abd El-Malak, Corrosion and inhibition of stainless steel pitting corrosion in alkaline medium and the effect of Cl^- and Br^- anions, Applied Surface Science 242 (1-2) (2005) 114–120.

[18] S. Refaey, F. Taha, A. Abd El-Malak, Inhibition of stainless steel pitting corrosion in acidic medium by 2-mercaptobenzoxazole, Applied Surface Science 236 (1-4) (2004) 175–185.

[19] G. Ilevbare, G. Burstein, The role of alloyed molybdenum in the inhibition of pitting corrosion in stainless steels, Corrosion Science 43 (3) (2001) 485–513.

[20] R. Qvarfort, Some observations regarding the influence of molybdenum on the pitting corrosion resistance of stainless steels, Corrosion Science 40 (2-3) (1998) 215–223.

[21] Z. Wang, A. Seyeux, S. Zanna, V. Maurice, P. Marcus, Chloride-induced alterations of the passive film on 316L stainless steel and blocking effect of pre-passivation, Electrochimica Acta 329 (2020) 135159.

[22] K. Hashimoto, K. Asami, K. Teramoto, An X-ray photo-electron spectroscopic study on the role of molybdenum in increasing the corrosion resistance of ferritic stainless steels in HCl, Corrosion Science 19 (1) (1979) 3–14.

[23] W. Yang, R.-C. Ni, H.-Z. Hua, A. Pourbaix, The behavior of chromium and molybdenum in the propagation process of localized corrosion of steels, Corrosion Science 24 (8) (1984) 691–707.

[24] H. Ogawa, H. Omata, I. Itoh, H. Okada, Auger electron spectroscopic and electrochemical analysis of the effect of alloying elements on the passivation behavior of stainless steels, Corrosion 34 (2) (1978) 52–60.

[25] A. Brooks, C. Clayton, K. Doss, Y. Lu, On the role of Cr in the passivity of stainless steel, Journal of the Electrochemical Society 133 (12) (1986) 2459–2464.

[26] M.-W. Tan, E. Akiyama, A. Kawashima, K. Asami, K. Hashimoto, The effect of air exposure on the corrosion behavior of amorphous Fe-8Cr-Mo-13P-7C alloys in 1 M HCl, Corrosion Science 37 (8) (1995) 1289–1301.

[27] K. Sugimoto, Y. Sawada, The role of molybdenum additions to austenitic stainless steels in the inhibition of pitting in acid chloride solutions, Corrosion Science 17 (5) (1977) 425–445.

[28] M. Bojinov, G. Fabricius, T. Laitinen, K. Mäkelä, T. Saario, G. Sundholm, Influence of molybdenum on the conduction mechanism in passive films on iron–chromium alloys in sulphuric acid solution, Electrochimica Acta 46 (9) (2001) 1339–1358.

[29] E. De Vito, P. Marcus, XPS study of passive films formed on molybdenum-implanted austenitic stainless steels, Surface and Interface Analysis 19 (1-12) (1992) 403–408.

[30] V. Maurice, H. Peng, L. H. Klein, A. Seyeux, S. Zanna, P. Marcus, Effects of molybdenum on the composition and nanoscale morphology of passivated austenitic stainless steel surfaces, Faraday discussions 180 (2015) 151–170.

[31] T. Massoud, V. Maurice, L. H. Klein, A. Seyeux, P. Marcus, Nanostructure and local properties of oxide layers grown on stainless steel in simulated pressurized water reactor environment, Corrosion Science 84 (2014) 198–203.

[32] L. Ma, F. Wiame, V. Maurice, P. Marcus, Origin of nanoscale heterogeneity in the surface oxide film protecting stainless steel against corrosion, npj Materials Degradation 3 (1) (2019) 1–9.

[33] Z. Wang, F. Di-Franco, A. Seyeux, S. Zanna, V. Maurice, P. Marcus, Passivation-induced physicochemical alterations of the native surface oxide film on 316L austenitic stainless steel, Journal of The Electrochemical Society 166 (11) (2019) C3376–C3388.

[34] Z. Wang, E.-M. Paschalidou, A. Seyeux, S. Zanna, V. Maurice, P. Marcus, Mechanisms of Cr and Mo enrichments in the passive oxide film on 316L austenitic stainless steel, Frontiers in Materials 6 (2019) 232.

[35] L. Ma, E.-M. Pascalidou, F. Wiame, S. Zanna, V. Maurice, P. Marcus, Passivation mechanisms and pre-oxidation effects on model surfaces of FeCrNi austenitic stainless steel, Corrosion Science 167 (2020) 108483.

[36] L. Ma, F. Wiame, V. Maurice, P. Marcus, Stainless steel surface structure and initial oxidation at nanometric and atomic scales, Applied Surface Science 494 (2019) 8–12.

[37] L. Ma, F. Wiame, V. Maurice, P. Marcus, New insight on early oxidation stages of austenitic stainless steel from in situ XPS analysis on single-crystalline Fe–18Cr–13Ni, Corrosion Science 140 (2018) 205–216.

[38] B. Lynch, Z. Wang, L. Ma, E.-M. Paschalidou, F. Wiame, V. Maurice, P. Marcus, Passivation-Induced Cr and Mo Enrichments of 316L Stainless Steel Surfaces and Effects of Controlled Pre-Oxidation, Journal of the Electrochemical Society 167 (14) (2020) 141509.

[39] T. Ohmi, Y. Nakagawa, M. Nakamura, A. Ohki, T. Koyama, Formation of chromium oxide on 316L austenitic stainless steel, Journal of Vacuum Science & Technology A: vacuum, surfaces, and films 14 (4) (1996) 2505–2510.

[40] Copyright © 2005 casa software ltd.
URL `http://www.casaxps.com/`

[41] P. Spevack, N. McIntyre, Thermal reduction of molybdenum trioxide, The Journal of Physical Chemistry 96 (22) (1992) 9029–9035.

[42] J. Högström, W. Fredriksson, K. Edstrom, F. Björefors, L. Nyholm, C.-O. A. Olsson, Cation profiling of passive films on stainless steel formed in sulphuric and acetic acid by deconvolution of angle-resolved X-ray photoelectron spectra, Applied Surface Science 284 (2013) 700–714.

[43] A. M. Salvi, J. E. Castle, J. F. Watts, E. Desimoni, Peak fitting of the chromium 2p XPS spectrum, Applied Surface Science 90 (3) (1995) 333–341.

[44] M. Aronniemi, J. Sainio, J. Lahtinen, Chemical state quantification of iron and chromium oxides using XPS: the effect of the background subtraction method, Surface Science 578 (1-3) (2005) 108–123.

[45] X. Wu, F. Wiame, V. Maurice, P. Marcus, 2-Mercaptobenzothiazole corrosion inhibitor deposited at ultra-low pressure on model copper surfaces, Corrosion Science (2020) 108464.

[46] J. Jia, A. Kara, L. Pasquali, A. Bendounan, F. Sirotti, V. A. Esaulov, On sulfur core level binding energies in thiol self-assembly and alternative adsorption sites: An experimental and theoretical study, The Journal of Chemical Physics 143 (10) (2015) 104702.

[47] P. Gobbo, M. C. Biesinger, M. S. Workentin, Facile synthesis of gold nanoparticle (AuNP)–carbon nanotube (CNT) hybrids through an interfacial Michael addition reaction, Chemical Communications 49 (27) (2013) 2831–2833.

[48] P. Keller, H.-H. Strehblow, XPS investigations of electrochemically formed passive layers on Fe/Cr-alloys in 0.5 M H_2SO_4, Corrosion Science 46 (8) (2004) 1939–1952.

[49] A. Grosvenor, B. Kobe, N. McIntyre, Examination of the oxidation of iron by oxygen using X-ray photoelectron spectroscopy and QUASESTM, Surface Science 565 (2-3) (2004) 151–162.

[50] P. C. Graat, M. A. Somers, Simultaneous determination of composition and thickness of thin iron-oxide films from XPS Fe 2p spectra, Applied Surface Science 100 (1996) 36–40.

[51] S. Roosendaal, B. Van Asselen, J. Elsenaar, A. Vredenberg, F. Habraken, The oxidation state of Fe (100) after initial oxidation in O_2, Surface Science 442 (3) (1999) 329–337.

[52] T.-C. Lin, G. Seshadri, J. A. Kelber, A consistent method for quantitative XPS peak analysis of thin oxide films on clean polycrystalline iron surfaces, Applied Surface Science 119 (1-2) (1997) 83–92.

[53] J.-G. Choi, L. Thompson, XPS study of as-prepared and reduced molybdenum oxides, Applied Surface Science 93 (2) (1996) 143–149.

[54] J. Baltrusaitis, B. Mendoza-Sanchez, V. Fernandez, R. Veenstra, N. Dukstiene, A. Roberts, N. Fairley, Generalized molybdenum oxide surface chemical state XPS determination via informed amorphous sample model, Applied Surface Science 326 (2015) 151–161.

[55] C. Clayton, Y. Lu, A bipolar model of the passivity of stainless steel: the role of Mo addition, Journal of the Electrochemical Society 133 (12) (1986) 2465–2473.

[56] I. Olefjord, The passive state of stainless steels, Materials Science and Engineering 42 (1980) 161–171.

[57] L. Wang, A. Seyeux, P. Marcus, Thermal stability of the passive film formed on 316L stainless steel surface studied by ToF-SIMS, Corrosion Science 165 (2020) 108395.

[58] P. Marcus, M. E. Bussell, XPS study of the passive films formed on nitrogen-implanted austenitic stainless steels, Applied Surface Science 59 (1) (1992) 7–21.

[59] Z. Wang, L. Zhang, X. Tang, Z. Zhang, M. Lu, The surface characterization and passive behavior of Type 316L stainless steel in H_2S-containing conditions, Applied Surface Science 423 (2017) 457–464.

[60] Y. Yan, M. Helfand, C. Clayton, Evaluation of the effect of surface roughness on thin film thickness measurements using variable angle XPS, Applied Surface Science 37 (4) (1989) 395–405.

[61] D. Mitchell, K. Clark, J. Bardwell, W. Lennard, G. Massoumi, I. Mitchell, Film thickness measurements of SiO_2 by XPS, Surface and Interface Analysis 21 (1) (1994) 44–50.

[62] P. J. Cumpson, The Thickogram: a method for easy film thickness measurement in XPS, Surface and Interface Analysis 29 (6) (2000) 403–406.

[63] P. Marcus, J. Grimal, The anodic dissolution and passivation of NiCrFe alloys studied by ESCA, Corrosion Science 33 (5) (1992) 805–814.

[64] Z. Wang, F. Di-Franco, A. Seyeux, S. Zanna, V. Maurice, P. Marcus, Passivation-induced physicochemical alterations of the native surface oxide film on 316L austenitic stainless steel, Journal of the Electrochemical Society 166 (11) (2019) C3376–C3388.

[65] W. Fredriksson, S. Malmgren, T. Gustafsson, M. Gorgoi, K. Edström, Full depth profile of passive films on 316L stainless steel based on high resolution HAXPES in combination with ARXPS, Applied Surface Science 258 (15) (2012) 5790–5797.